Effect of the Inhomogeneity of Ice Crystals on Retrieving Ice Cloud Optical Thickness and Effective Particle Size

Yu Xie* and Ping Yang

Department of Atmospheric Sciences, Texas A&M University, College Station, TX 77843

George W. Kattawar

Department of Physics, Texas A&M University, College Station, TX 77843

Patrick Minnis and Yong X. Hu

NASA Langley Research Center, Hampton, VA 23681

For publication in the

Journal of Geophysical Research

* *Corresponding author address:* Yu Xie, Department of Atmospheric Sciences, Texas A&M University, College Station, TX 77843; Tel: 979-458-0544

Email: xieyu@ariel.met.tamu.edu

Abstract

Spherical or spheroidal air bubbles are generally trapped in the formation of rapidly growing ice crystals. In this study the single-scattering properties of inhomogeneous ice crystals containing air bubbles are investigated. Specifically, a computational model based on an improved geometric-optics method (IGOM) has been developed to simulate the scattering of light by randomly oriented hexagonal ice crystals containing spherical or spheroidal air bubbles. A combination of the ray-tracing technique and the Monte Carlo method is used. The effect of the air bubbles within ice crystals is to smooth the phase functions, diminish the 22° and 46° halo peaks, and substantially reduce the backscatter relative to bubble-free particles. These features vary with the number, sizes, locations and shapes of the air bubbles within ice crystals. Moreover, the asymmetry factors of inhomogeneous ice crystals decrease as the volume of air bubbles increases. Cloud reflectance lookup tables were generated at wavelengths 0.65 μm and 2.13 μm with different air-bubble conditions to examine the impact of the bubbles on retrieving ice cloud optical thickness and effective particle size. The reflectances simulated for inhomogeneous ice crystals are slightly larger than those computed for homogenous ice crystals at a wavelength of 0.65 μm. Thus, the retrieved cloud optical thicknesses are reduced by employing inhomogeneous ice cloud models. At a wavelength of 2.13 μm, including air bubbles in ice cloud models may also increase the reflectance. This effect implies that the retrieved effective particle sizes for inhomogeneous ice crystals are larger than those retrieved for homogeneous ice crystals, particularly, in the case of large air bubbles.

1. Introduction

An appropriate representation of cirrus clouds in radiative transfer simulations has long been a subject of great interest, not only because of their importance for cloud radiative forcing and energy budget of the earth, but also because of the uncertainties associated with the shapes and sizes of ice crystals within these clouds [*Ramanathan et al.*, 1983; *Liou*, 1986; Baran, 2004]. Heymsfield and Platt [1984] and Heymsfield [1977] developed representative data sets for cirrus cloud particles based on in situ measurements. The ice crystal samples, collected both in late winter and spring, showed that hexagonal hollow columns and solid columns were predominant at temperatures below 223K. Some other particle habits, such as hexagonal plates and bullet rosettes were also observed at the top of ice clouds.

Although approximating the single-scattering properties (e.g., phase function, single-scattering albedo, and asymmetry factor) of realistic ice crystals by assuming one idealized geometrical shape is an oversimplification [*Foot*, 1988], it is significantly better for retrieving ice cloud properties than assuming that the clouds are composed of spherical ice crystals [*Minnis et al.*, 1993]. But, a more accurate representation of cirrus cloud ice crystal properties is needed. For example, the use of homogeneous hexagonal ice crystals [*Minnis et al.*, 1998] can yield accurate estimates of ice water path [*Mace et al.*, 2005], but the retrieved optical depths tend to be too low [*Min et al.*, 1994] implying overestimates of the effective particle size. To further improve the representation of cloud ice crystals in radiative transfer calculations, steady progress has been made toward single-scattering computations involving various complex particle shapes away from the simple single shape. *Liou* [1972] first assumed non-spherical ice crystals as long circular cylinders, who showed significant differences in the comparison of the phase functions for polydisperse spheres and the counterparts for long circular cylinders. *Takano and Liou* [1989], *Muinonen* [1989], *Brorovoi and Grishin* [2003] and many others applied the traditional ray-tracing method or its modified forms to the scattering by randomly and horizontally oriented hexagonal particles. The optical properties of various complicated ice crystals have been simulated by *Macke* [1993], *Macke et al.* [1996], *Iaquinta et al.* [1995], *Takano and Liou* [1995], *Yang and Liou* [1998], *Um and McFarquhar* [2007], and *Schmitt et al.* [2006]. *Yang and Liou* [1996] employed the finite-difference time domain (FDTD) method to simulate the scattering of light by small bullet-rosettes, hexagonal plates, solid columns, and hollow columns. Recently, the optical properties of highly complex habits, such as ice crystals with surface roughness and hollow bullet rosette ice crystals, have been investigated [*Yang et al.*, 2008 a, b; *Yang et al.*, in press]. The results from these efforts have been used in the simulation of radiative transfer in cirrus clouds.

Homogeneous ice crystals are extensively employed in the aforementioned studies of the single-scattering properties of irregular ice particles. In the accretion and aggregation of ice crystals, an ice particle may collide with supercooled water droplets or other ice particles. When this happens, ice crystals can rapidly grow and form large ice crystals. The collision and coalescence processes may lead to the trapping of spherical or spheroidal air bubbles within ice crystals when the supercooled water droplets freeze almost instantly [*Tape*, 1994]. Air bubbles may also originate when water containing dissolved air freezes into ice crystals. *Hallett* [1964] showed that supercooled water turns into ice by solidifying the remainder from outside but the process is quite slow. This inward growth of the ice may cause the originally dissolved air to be released and subsequently form small bubbles in the center of the ice particle. The size and concentration of air bubbles are then influenced by the rate of freezing, amount of dissolved air in water, and temperature during the freezing process [*Carte*, 1961; *Hallett*, 1964].

There are only a handful of studies reported on the optical properties of inhomogeneous ice crystals because of the lack of laboratory and in situ measurements and difficulties in specifying the inclusion shapes. Among these previous studies, *Macke et al.* [1996] employed a combination of the ray-tracing and Monte Carlo techniques to investigate the single-scattering properties of randomly oriented hexagonal columns containing ammonium sulfate, air bubbles, and soot impurities. In their computations, the scattering events at the outer boundary of the hexagonal particle are considered by using the ray-tracing technique [*Macke et al.* 1993], whereas the Monte Carlo method is used to account for the photon propagation directions affected by the internal inclusions. *Yang et al.* [2000] used the FDTD technique to compute the scattering phase functions of ice crystals with inclusions of soot impurities and air bubbles. *Labonnote et al.* [2001] developed an Inhomogeneous Hexagonal Monocrystals (IHM) model for ice crystals containing randomly located air bubbles. This single-scattering property model, based on the ray-tracing and Monte Carlo techniques developed by *Macke et al.* [1996], has further defined the internal air bubbles in terms of spherical voids with a size distribution. Studies on the microphysical and optical properties of ice clouds were carried out by *Labonnote et al.* [2001] and *Knap et al.* [2005], who used the IHM model to investigate the bulk-scattering properties of ice clouds and to compare the simulations with satellite-based measurements of polarized radiances.

The IHM model does not account for the case where an ice crystal contains only a few air bubbles with specific locations. The geometries of air bubbles in the previous studies are restricted to be spheres, a constraint that is not always realistic. This paper reports on a new inhomogeneous ice crystal model based on the surface observations reported by *Tape* [1994]. Furthermore, the effect of the air bubbles on the retrieval of cloud optical thickness and effective particle sizes is investigated. This paper is organized as follows. In Section 2, we describe the morphologies of ice crystals observed by *Tape* [1994] and define the geometries of the inhomogeneous ice crystals for the present scattering computations. Then, we introduce the single-scattering model based on an improved geometrical-optics method (IGOM). In Section 3, we illustrate the effect of the number, shape, size, and location of the air bubbles inside hexagonal ice crystals on the single-scattering properties of these particles. In Section 4, we show ice cloud bidirectional reflectance as a function of the effective particle size, optical thickness, and solar and satellite viewing angles, which is computed from the inhomogeneous ice crystal model. Moreover, we derive cloud microphysical and optical properties based on the Moderate Resolution Imaging Spectroradiometer (MODIS) measurements and compare the retrieval results from homogeneous and inhomogeneous ice crystal models. The conclusions and discussions of this study are given in Section 5.

2. Single-scattering model for inhomogeneous ice crystals

Although the geometries of ice crystals in the atmosphere have been extensively studied using airborne in situ observations [*Korolev and Isaac*, 1999; *Heymsfield and Platt*, 1984; *McFarquhar and Heymsfield*, 1996], ground-based observations also provide useful data for investigating ice crystal morphologies. *Tape* [1983, 1994] used Petri dishes containing hexane or silicone oil and acrylic spray to collect ice crystals falling near the surface and observed the ice crystal shapes using a binocular microscope. Figure 1 illustrates the ice crystals sampled by *Tape* [1994] at the South Pole on January 19, 1985 and January 17, 1986. In the photographs, the ice crystals have typical hexagonal shapes and most of these particles are inhomogeneous with air bubbles inside. The inhomogeneous ice crystal morphologies observed at the surface are consistent with those from airborne observations. The observed inhomogeneous ice crystals spurred development of the theoretical models used by *Macke et al.* [1993] and *Labonnote et al.* [2001] to compute the single-scattering properties of these particles. However, unlike the crystal geometries in the IHM model [*Labonnote et al.* 2001], an inhomogeneous ice crystal contains a few air bubbles with visible dimensions. The sizes of the air bubbles are relatively large, as the maximum dimensions of the air bubbles are comparable with the width of the ice crystal. Another significant difference between the observations by *Tape* [1994] and the IHM model is that the actual air bubbles are not always spheres, although most of them have spherical shapes. Moreover, the air bubbles are located almost exclusively along the vertical axes of the hexagons in the center of hexagonal columns. However, for hexagonal plates, more than one air bubble can be horizontally aligned near the surface of the particles.

Based on the ice particles photographed by *Tape* [1994], the geometries of inhomogeneous ice crystals in this study are defined as those shown in Fig. 2. For hexagonal columns, only one or two air bubbles are included within ice particles. Furthermore, the air bubble inclusions in our model are all on the axes of ice crystals (see the upper and middle panels in Fig. 2). For hexagonal plates, the air bubbles are aligned horizontally if more than one air bubble is included (see the lower panels in Fig. 2). The orientations of ice crystals for either hexagonal columns or plates are specified in the OXYZ coordinate system denoted in Fig. 3. Following *Yang and Liou* [1996], the Y-axis in Fig. 3 is perpendicular to one of the ice crystal's side faces, and the Z-axis is along the vertical axis of the hexagon. The shape of an air bubble is defined in terms of the following equation:

$$\frac{(x-x_r)^2}{r_1^2}+\frac{(y-y_r)^2}{r_2^2}+\frac{(z-z_r)^2}{r_3^2}=1, \qquad (1)$$

where r_1, r_2, and r_3 are the three semi-axes along the X, Y and Z axes, respectively, and the coordinates (x_r, y_r, z_r) specify the center of the air bubble in the OXYZ system.

In this study, the IGOM [*Yang and Liou*, 1996] based on the ray-tracing technique is used to compute the single-scattering properties of inhomogeneous ice crystals. At the outer boundary of the inhomogeneous ice crystals, the computation of reflection and refraction events is the same as in the case for homogeneous hexagonal ice crystals. Detailed descriptions of the IGOM method are reported in *Yang and Liou* [1996].

If a ray is refracted into an ice crystal, the next step is to trace the refracted ray and determine if it is intersected by any air bubble within the particle. Figure 4 shows the flow-chart for reflection and refraction by internal air bubbles. For an air bubble with the particle shape given by Eq. (1), the coordinates of the incident point B, (x_b, y_b, z_b), can be determined as follows:

$$x_b = x_a + (\hat{e} \cdot \hat{x})l, \tag{2}$$

$$y_b = y_a + (\hat{e} \cdot \hat{y})l, \tag{3}$$

$$z_b = z_a + (\hat{e} \cdot \hat{z})l, \tag{4}$$

where the coordinates (x_a, y_a, z_a) indicate the position of the first incident point A at the ice crystal surface, $\hat{e}$ is a unit vector along the incident direction, $\hat{x}$, $\hat{y}$, and $\hat{z}$ are the unit vectors along the X, Y, and Z axes, respectively, and l is the distance between points A and B. Substituting Eqs. (2)-(4) into Eq. (1), we obtain

$$A_1 l^2 + A_2 l + A_3 = 0, \tag{5}$$

where

$$A_1 = r_2^2 r_3^2 (\hat{e} \cdot \hat{x})^2 + r_1^2 r_3^2 (\hat{e} \cdot \hat{y})^2 + r_1^2 r_2^2 (\hat{e} \cdot \hat{z})^2, \tag{6}$$

$$A_2 = 2 r_2^2 r_3^2 (x_a - x_r)(\hat{e} \cdot \hat{x}) + 2 r_1^2 r_3^2 (y_a - y_r)(\hat{e} \cdot \hat{y}) + 2 r_1^2 r_2^2 (z_a - z_r)(\hat{e} \cdot \hat{z}), \tag{7}$$

$$A_3 = r_2^2 r_3^2 (x_a - x_r)^2 + r_1^2 r_3^2 (y_a - y_r)^2 + r_1^2 r_2^2 (z_a - z_r)^2 - r_1^2 r_2^2 r_3^2 . \tag{8}$$

A ray will intercept an air bubble when A_1, A_2, and A_3 satisfy

$$A_2^2 - 4 A_1 A_3 > 0, \tag{9}$$

and

$$\frac{-A_2 - \sqrt{A_2^2 - 4 A_1 A_3}}{2 A_1} > 0 . \tag{10}$$

The directions of the reflected and refracted rays, $\hat{e}_r$ and $\hat{e}_t$ can be determined on the basis of Snell's law in the form of

$$\hat{e}_r = \hat{e} - 2(\hat{e} \cdot \hat{n})\hat{n}, \tag{11}$$

$$\hat{e}_t = N_r[\hat{e} - (\hat{e} \cdot \hat{n})\hat{n} - \sqrt{N_r^{-2} - 1 + (\hat{e} \cdot \hat{n})^2}\,\hat{n}], \tag{12}$$

where N_r is the real part of an adjusted refractive index that has been formularized by *Yang and Liou* [1995] and $\hat{n}$ is the normal direction of the air-bubble surface at point B. For spheroidal air bubbles used in this study, $\hat{n}$ can be given by

$$\hat{n}_x = \frac{2(x_b - x_r)}{r_1^2} \Bigg/ \sqrt{\left[\frac{2(x_b - x_r)}{r_1^2}\right]^2 + \left[\frac{2(y_b - y_r)}{r_2^2}\right]^2 + \left[\frac{2(z_b - z_r)}{r_3^2}\right]^2}, \tag{13}$$

$$\hat{n}_y = \frac{2(y_b - y_r)}{r_2^2} \Bigg/ \sqrt{\left[\frac{2(x_b - x_r)}{r_1^2}\right]^2 + \left[\frac{2(y_b - y_r)}{r_2^2}\right]^2 + \left[\frac{2(z_b - z_r)}{r_3^2}\right]^2} \tag{14}$$

$$\hat{n}_z = \frac{2(z_b - z_r)}{r_3^2} \Bigg/ \sqrt{\left[\frac{2(x_b - x_r)}{r_1^2}\right]^2 + \left[\frac{2(y_b - y_r)}{r_2^2}\right]^2 + \left[\frac{2(z_b - z_r)}{r_3^2}\right]^2}. \tag{15}$$

For the ray refracted into the air bubble, the next impinging point C, (x_c, y_c, z_c), on the air-bubble surface can be determined as follows:

$$x_c = x_b + (\hat{e}_t \cdot \hat{x})l', \tag{16}$$

$$y_c = y_b + (\hat{e}_t \cdot \hat{y})l', \tag{17}$$

$$z_c = z_b + (\hat{e}_t \cdot \hat{z})l', \tag{18}$$

where l' is the distance between points B and C. l' can be solved from Eqs. (5)-(8) by replacing l and $\hat{e}$ by l' and $\hat{e}_t$, respectively.

If the conditions in Eqs. (9) and (10) are not satisfied, i.e., the incident ray does not impinge upon the air bubble centered at (x_r, y_r, z_r), the process above will be repeated for another air bubble if more than one air bubble is embedded in the ice crystal of interest.

3. Single-scattering properties of inhomogeneous ice crystals

Figure 5 compares the scattering phase functions for homogeneous ice crystals with their inhomogeneous ice crystal counterparts at wavelengths λ, 0.65 and 2.13 μm. The refractive indices of ice at wavelengths 0.65 and 2.13 μm are $1.3080 + i1.43\times10^{-8}$ and $1.2673 + i5.57\times10^{-4}$, respectively. The ice crystals are assumed to be randomly oriented hexagonal columns and plates with the aspect ratios, $2a/L$=80 μm/100 μm and 100 μm/43 μm, respectively, where a is the radius of a cylinder that circumscribes the hexagonal ice particle and L is the length of the ice particle. Specifically, Fig. 5a shows the phase functions at λ=0.65 μm for homogeneous hexagonal columns and inhomogeneous columns with the same aspect ratio. For the two inhomogeneous conditions, spherical air bubbles with radii of 16 or 34 μm are centered at the centers of ice crystals. It is then evident from Fig. 5a that the air bubbles within ice crystals can greatly affect the scattering properties of ice particles. In the homogeneous case, the pronounced 22° and 46° halo peaks are quite pronounced as the typical features of the phase functions for homogeneous hexagonal ice crystals. However, the magnitudes of the peaks at the scattering angles 22° and 46° are reduced if small air bubbles with a radius of 16 μm is embedded in the crystals. For ice crystals containing relatively large air bubbles with a radius of 34 μm, the pronounced 22° and 46° peaks are more significantly smoothed out in the scattering phase function although they are still slightly noticeable. Furthermore, the backscattering is substantially reduced in the inhomogeneous case. It should be noted that a bubble embedded in ice acts as a diverging lens and affects internal rays; however, the forward peaks are essentially unaffected by bubbles since diffraction is the primary cause and depends primarily on the particle projected area. Figure 5b shows the scattering phase functions for homogeneous and inhomogeneous hexagonal columns at λ=2.13 μm. The effect of air bubbles at the near-infrared wavelength is similar to that in the case for visible wavelengths. Figure 5c shows the scattering phase functions of hexagonal plates at λ=0.65 μm. In this panel, the dotted line describes the phase function for inhomogeneous ice crystals containing a spherical air bubble with a radius of 21.25 μm. For the other inhomogeneous case, four identical air bubbles are aligned parallel to the basal faces of the plates. Similar to the effect in the hexagonal columns, the trapped air bubbles in hexagonal plates smooth the scattering phase function and reduces the back scattering. However, the scattering phase function is not sensitive to the increase of the number of air bubbles in hexagonal plates. A similar effect of air bubbles on the single-scattering properties is also seen in Fig. 5d for wavelength 2.13 μm.

Figure 6 shows the degrees of linear polarization, $-p_{12}/p_{11}$, for ice crystals having the same aspect ratios and inhomogeneity as in Fig. 5. Figures 6a and 6b compare the degrees of linear polarization between homogeneous and inhomogeneous hexagonal columns. It is seen that air bubbles embedded within ice crystals can also reduce the magnitude of the degrees of linear polarization, particularly, in the case for large air bubbles. The same effect can also be found for hexagonal plates, whose scattering phase functions are shown in Figures 6c and 6d at λ=0.65 μm and λ=2.13 μm, respectively. However, unlike the performance of scattering phase functions in Fig. 5, increasing the number of air bubbles in hexagonal plates may lead to more significant smoothing of the degree of linear polarization.

Figure 7 shows the phase matrices for hexagonal columns at λ=0.65 μm. For one of the inhomogeneous ice crystals, a spherical air bubble with radius of 21.25 μm is included in a hexagonal column whose aspect ratio is 2a/L=50 μm /100 μm. To specify the effect of the shapes of air bubbles on the single-scattering properties of ice crystals, volume-equivalent spheroids are considered in the other type of ice crystals with the same aspect ratio. It is evident from Fig. 7 that spherical air bubbles have a greater effect on the phase matrix than those containing spheroidal air bubbles. This feature is physically understandable since for the same volume, a spherical particle has a larger cross section than a spheroid. Then the incident photon has a greater chance to be intercepted by spherical air bubbles than their counterparts with other shapes. In addition to the phase function and degree of linear polarization, the other elements of the phase matrix are also sensitive to the presence of air bubbles.

To further illustrate the effect of air bubbles on the single-scattering properties of ice crystals, Fig. 8 shows the asymmetry factor as a function of the volume of the air bubbles at λ=0.65 μm and λ=2.13 μm. The aspect ratio of ice crystals is 2a/L=10 μm /50 μm. Spheroidal air bubbles are located in the center of the ice crystals where the r_1 and r_2 in Eq. (1) are both 4.25 μm. The relative volume of the air bubble, V_b/V, can be specified in terms of r_3 in Eq. (1), where V_b and V are the volumes of the air bubbles and ice crystals, respectively. It is seen from Fig. 8 that the asymmetry factors decrease with increasing V_b/V at both visible and near-infrared wavelengths.

4. Effect of inhomogeneous ice crystals on ice cloud retrieval

To study the effect of inhomogeneous ice crystals on retrieving ice cloud properties, aspect ratios of ice crystals as well as particle size distributions in ice clouds are required. In this sensitivity study, an aspect ratio of 2a/L=0.2 is used for all ice crystals, although it may not correspond well to observations [*Ono*, 1969]. Furthermore, small (r_1=0.45a, r_2=0.45a, and r_3=0.2L) and relatively large (r_1=0.85a, r_2=0.85a, and r_3=0.2L) air bubbles are defined at the center of each inhomogeneous ice crystal. The size distribution of ice crystals is assumed to obey a Gamma distribution given by

$$n(L) = N_0 L^{\mu} \exp(\frac{b + \mu + 0.67}{L_m} L), \qquad (19)$$

where N_0 is the intercept, μ is assumed to be 2 in this study, and L_m is the median of the distribution of L. The parameter b is taken to be 2.2. The effective particle size for a given size distribution is defined as follows [*Foot*, 1988]:

$$r_e = \frac{3\int_{L_{\min}}^{L_{\max}} V(L)n(L)dL}{4\int_{L_{\min}}^{L_{\max}} A(L)n(L)dL}, \qquad (20)$$

where V is particle volume, and A is projected area.

The ice cloud bi-directional reflectances are computed using the Discrete Ordinates Radiative Transfer (DISORT) model for λ = 0.65 and 2.13 μm at various incident-scattering configurations. The visible optical thickness at λ = 0.65 μm serves as the reference optical thickness in this study. The optical thickness for a given wavelength is related to the visible optical thickness via

$$\tau = \frac{\tau_{vis} Q}{Q_{vis}}, \qquad (21)$$

where Q and Q_{vis} are the extinction efficiencies for λ=2.13 and 0.65 μm, respectively.

Figure 9a shows the comparison of the lookup tables computed for the solid homogeneous ice crystals and the inhomogeneous ice crystals containing small air bubbles (r_1= r_2=0.45a, and r_3=0.2L). It is seen that the inhomogeneous ice crystals reflect slightly more than the homogeneous ice crystals at λ = 0.65 μm whereas the bi-directional reflectances for the inhomogeneous ice crystals are significantly larger than those for the homogeneous particles at λ = 2.13 μm. Figure 9b is the same as Fig. 9a except that each inhomogeneous ice crystal in Fig. 9b contains bigger air bubbles with radii of r_1= r_2=0.85a, and r_3=0.2L. It is then evident that the bidirectional reflectances at λ = 0.65 μm are slightly sensitive to the air bubble size. However, large air bubbles in the ice crystals can significantly increase the reflectances at λ = 2.13 μm.

The left and right panels in the top of Fig. 10 show a MODIS granule image over the south Pacific Ocean on April 17, 2007 and the cloud mask from the operational MODIS cloud product, respectively. The middle and bottom panels of Fig. 10 show the retrieved cloud properties for the pixels that have been identified as covered by ice clouds. Specifically, the middle panel on the left compares the retrieved ice cloud optical thickness from homogeneous and inhomogeneous ice crystals. For the latter, small air bubbles (r_1= r_2=0.45a, and r_3=0.2L) are embedded. The middle panel on the right is the same with the left panel except that the inhomogeneous ice crystals have larger air bubbles (r_1= r_2=0.85a, and r_3=0.2L). It is then evident that the cloud optical thicknesses are slightly reduced by using inhomogeneous ice crystal models in ice cloud property retrievals. These results are consistent with Fig. 9 where the inhomogeneous ice crystals reflect more than homogeneous ice crystals at λ = 0.65 μm. The increase of the sizes of air bubbles can further reduce the optical thickness as evident from the comparison of the two middle panels in Fig. 10. Using inhomogeneous ice crystals in ice cloud models may significantly increase the retrieved ice cloud effective particle sizes, as evident from the bottom panels in Fig. 10. Moreover, this effect becomes more significant as sizes of the air bubbles increase.

Figures 9 and 10 describe the sensitivities of ice cloud reflectance and cloud property retrievals to optical properties of inhomogeneous ice crystals. In this study, the same particle volumes and size distributions are employed for both homogeneous and inhomogeneous ice crystals. However, containing air bubbles contained in ice crystals will decrease the volume of ice and therefore decrease the effective particle size of ice crystals in the ice cloud. Figure 11 shows the variations of effective particle sizes with the volumes of the air bubbles within ice crystals. It is seen that the effective particle sizes of ice clouds can be reduced to more than 50%, depending on the shape and size of the air bubbles within ice crystals. Thus, the increased effective particle sizes resulting from a retrieval employing inhomogeneous ice crystals in Fig. 10 can be partly compensated if the volumes of the air bubbles are subtracted from the particle volumes.

5. Summary

This study reports on the single-scattering properties of inhomogeneous ice crystals whose geometries are defined based on the observations made by *Tape* [1994] at the South Pole. Unlike the spherical air bubbles with random locations in the IHM model previously developed by *Labonnote et al.* [2001], in the present study a few spherical or spheroidal air bubbles are defined at the center of hexagonal ice crystals. The sensitivity of single-scattering properties to inhomogeneous ice crystals has been examined. It is found that the single-scattering phase function is smoothed out and its peaks at the scattering angles 22° and 46° are reduced if air bubbles are included in the ice crystals. These features have been previously reported [*Labonnote et al.*, 2001; *Macke et al.*, 1996]. The phase function smoothing can become more pronounced by increasing the number of air bubbles, enlarging the air bubbles, changing the air bubbles' shapes from spheroids to spheres, or moving them from the sides to the center of an ice crystal. The peaks of the degrees of linear polarization can also be reduced by considering inhomogeneous ice crystals. Moreover, the asymmetry factors of inhomogeneous ice crystals decrease as the relative volume of the air bubbles increases.

Furthermore, a lookup library of bidirectional reflectances has been developed for both homogenous and homogenous ice cloud models at λ = 0.65 and 2.13 μm. We showed that using inhomogeneous ice cloud models can increase the bidirectional reflectances at those two wavelengths. Therefore, the retrieved ice cloud optical thicknesses are slightly reduced whereas the retrieved ice cloud effective particle sizes can be significantly increased by including air bubbles in ice crystals, particularly, in the case of large air bubbles. This effect is similar to that found when surface roughness is included in the computations of ice crystal single-scattering properties [*Yang et al.*, 2008a,b], except that the presence of air bubbles in the crystals reduces the overall ice water content compared to a solid crystal with roughened surfaces. These results represent another important step in the effort to develop realistic ice crystal optical properties for use in retrieving ice cloud properties from satellite imagery and representing them in numerical weather and climate models. The results appear to be in the right direction for decreasing the biases in retrieved ice cloud optical properties, .e.g., *Min et al.* [2004]. Additional study will be needed, however, to determine if the optical properties of spheroidal bubbles, either alone or in combination with those for other ice crystal formulations, can provide a more accurate representation of actual ice crystal reflectance behavior.

Acknowledgements

This research is supported by a National Science Foundation (NSF) grant (ATM-0239605) managed by Dr. Bradley Smull and by a NASA grant (NNL06AA23G). George W. Kattawar's research is also supported by the Office of Naval Research under contract N00014-06-1-0069. Patrick Minnis is supported through the NASA Radiation Sciences Program and the NASA Clouds and the Earth's Radiant Energy System Project.

References

Baran, A. J. (2004), On the scattering and absorption properties of cirrus cloud, *J. Quant. Spectrosc. Radiat. Transfer,* 89, 17-36.

Borovoi, A. G., and I. A. Grishin (2003), Scattering matrices for large ice crystal particles, *J. Opt. Soc. Am. A.*, 20, 2071-2080.

Carte, A. E. (1961), Air bubbles in ice, *Proc. Phys. Soc.*, 77, 757-768.

Foot, J. S. (1988), Some observations of the optical properties of clouds. II: Cirrus, *Q. J. R. Meteorol. Soc.*, 114, 145-169.

Hallett, J. (1964), Experimental studies of the crystallization of supercooled water, *J. Atmos. Sci.*, 21, 671-682.

Heymsfield, A. J. (1977), Precipitation development in stratiform ice clouds: A microphysical and dynamical study, *J. Atmos. Sci.*, 34, 367-381.

Heymsfield, A. J and C. M. R. Platt (1984), A parameterization of the particle size spectrum of ice clouds in terms of the amient temperature and the ice water content, *J. Atmos. Sci.*, 41, 846-855.

Iaquinta, J., H. Isaka, and P. Personne (1995), Scattering phase function of bullet rosette ice crystals, *J. Atmos. Sci.,* 52, 1401-1413.

Knap, W. H., L. C. Labonnote, G. Brognlez, and P. Stammes (2005), Modeling total and polarized reflectances of ice clouds: evaluation by means of POLDER and ATSR-2 measurements, *Appl. Opt.,* 44, 4060-4073.

Korolev, A. V., G. A. Isaac, and J. Hallett (1999), Ice particle habits in Arctic clouds, *Geophy. Res. L.*, 26, 1299-1302.

Labonnote, L. C., G. Brogniez, J. C. Buriez, and M. Doutriaux-Boucher (2001), Polarized light scattering by inhomogeneous hexagonal monocrystals: validation with ADEOS-POLDER measurements, *J. Geophy. Res.*, 106, 12139-12155.

Liou, K. N. (1972), Light scattering by ice clouds in the visible and infrared: a theoretical study, *J. Atmos, Sci.,* 29, 524-536.

Liou, K. N. (1986), Influence of cirrus clouds on weather and climate processes: A global perspective, *Mon. Wea. Rev*., 114, 1167-1199.

Mace, G. G., Y. Zhang, S. Platnick, M. D. King, P. Minnis, and P. Yang (2005), Evaluation of cirrus cloud properties from MODIS radiances using cloud properties derived from ground-based data collected at the ARM SGP site, *J. Appl. Meteorol.*, *44*, 221-240.

Macke, A. (1993), Scattering of light by polyhedral ice crystals, *Appl. Opt.*, 32, 2780-2788.

Macke, A., M. I. Mishchenko, and B. Cairns (1996), The influence of inclusions on light scattering by large ice particles, *J. Geophys. Res*., 101, 23311-23316.

Macke, A. J. Mueller, and E. Raschke (1996), Single scattering properties of atmospheric ice crystal, *J. Atmos. Sci*., 53, 2813-2825.

McFarquhar, G. M. and A. J. Heymsfield (1996), Microphysical characteristics of three Anvils sampled during the Central Equatorial Experiment, *J. Atmos. Sci.*, 53, 2401-2423.

Min, Q, P. Minnis, and M. M. Khaiyer (2004), Comparison of cirrus optical depths from GOES-8 and surface measurements, *J. Geophys. Res.*, *109*, D20119, 10.1029/2003JD004390.

Minnis, P., D. P. Garber, D. F. Young, R. F. Arduini, and Y. Takano (1998), Parameterization of reflectance and effective emittance for satellite remote sensing of cloud properties, *J. Atmos. Sci.*, *55*, 3313-3339.

Minnis, P., P. W. Heck, and D. F. Young (1993), Inference of cirrus cloud properties using satellite-observed visible and infrared radiances, Part II: Verification of theoretical cirrus radiative properties, *J. Atmos. Sci.*, *50*, 1305-1322.

Mishchenko, M. I., J. W. Hovenier and L. D. Travis (2000), *Light scattering by nonsphericial particles*, Academic press, San Diego, San Francisco, New York, Boston, London, Sydney, Tokyo.

Muinonen, K. (1989), Scattering of light by crystals: a modified Kirchhoff approximation, *Appl. Opt.*, 28, 3044-3050.

Nakajima T. and M. D. King (1990), Determination of the optical thickness and effective particle radius of clouds from reflected solar radiation measurements. Part I: Theory, *J. Atmos. Sci.*, 47, 1878-1893.

Ono, A. (1969), The shape and riming properties of ice crystals in natural clouds, *J. Atmos. Sci.*, 26, 138-147.

Ramanathan, V., E. J. Pitcher, R. C. Malone, and M. L. Blackmon (1983), The response of a general circulation model to refinements in radiative processes, *J. Atmos. Sci.*, 40, 605-630.

Schmitt, C. G., J. Iaquinta, and A. J. Heymsfield (2006), The asymmetry parameter of cirrus clouds composed of hollow bullet rosette–shaped ice crystals from ray-tracing calculations. *J. Appl. Meteor. and Climat.*, 45, 973–981.

Takano, Y and K. N. Liou (1989), Solar radiative transfer in cirrus clouds. Part I: single-scattering and optical properties of hexagonal ice crystals, *J. Atmos. Sci.*, 46, 3-19.

Takano, Y. and K.N. Liou (1995), Radiative transfer in cirrus clouds. III. Light scattering by irregular ice crystals, *J. Atmos. Sci.*, 52, 818-837.

Tape, W. (1983), Some ice crystals that made halos, *J. Opt. Soc. Am.*, 73, 1641-1645.

Tape, W. (1994), *Atmospheric halos*, American Geophysical Union, Washington, D. C., USA.

Um, J., and G. M. McFarquhar (2007), Single-Scattering Properties of Aggregates of Bullet Rosettes in Cirrus, *J. Appl. Meteor. and Climatology*, 46, 757–775.

Yang P., G. Hong, G. W. Kattawar, P. Minnis and Y. X. Hu (2008a), Uncertainties associated with the surface texture of ice particles in satellite-based retrieval of cirrus clouds: Part II. Effect of particle surface roughness on retrieved cloud optical thickness and effective particle size, *Geo. Remote. Sens.*, 46, 1948-1957.

Yang, P., G. W. Kattawar, G. Hong, P. Minnis and Y. X. Hu (2008b), Uncertainties associated with the surface texture of ice particles in satellite-based retrieval of cirrus clouds: Part I. Single-scattering properties of ice crystals with surface roughness, *Geo. Remote. Sens.*, 46, 1940-1947.

Yang, P and K. N. Liou (1995), Light scattering by hexagonal ice crystals: comparison of finite-difference time domain and geometric optics models, *J. Opt. Soc. Am.*, A12, 162-176.

Yang, P. and K. N. Liou (1996), Finite-difference time domain method for light scattering by small ice crystals in three-dimensional space, *J. Opt. Soc. Amer.*, A13, 2072-2085.

Yang, P., and K. N. Liou (1998), Single-scattering properties of complex ice crystals in terrestrial atmosphere, *Contr. Atmos. Phys.*, 71, 223-248.

Yang, P., K. N. Liou, M. I. Mishchenko, and B. C. Gao (2000), An efficient finite-difference time domain scheme for light scattering by dielectric particles: application to aerosols, *Appl. Opt.*, 39, 3727-3737.

Yang, P., Z. B. Zhang, G. W. Kattawar, S. G. Warren, B. A. Baum, H. L. Huang, Y. X. Hu, D. Winker, and J. Iaquinta (in press), Effect of cavities on the optical properties of bullet rosettes: Implications for active and passive remote sensing of ice cloud properties, J. Appl. Meteorol. Climatol..

Figure Captions

Fig. 1. Inhomogeneous ice crystals sampled by Walter Tape [Tape, 1994] at the South Pole, on January 19, 1985 (left) and January 17, 1986 (right).

Fig. 2. The geometries of inhomogenous ice crystals.

Fig. 3 Geometry of a hexagonal ice crystal with an air bubble inside.

Fig. 4. Schematic flow-chart for reflection and refraction by internal air bubbles.

Fig. 5. Scattering phase functions for homogeneous and inhomogeneous ice crystals at λ=0.65 μm (panels a and c) and 2.13 μm (panels b and d).

Fig. 6. Degrees of linear polarization for homogeneous and inhomogeneous ice crystals at λ=0.65 μm (panels a and c) and 2.13 μm (panels b and d). The ice crystals' sizes and morphologies in this figure are the same as those in Fig. 5.

Fig. 7. Scattering phase matrixes for homogeneous and inhomogeneous ice crystals at λ=0.65 μm.

Fig. 8. Asymmetry factors for inhomogeneous ice crystals at λ=0.65 μm (left) and 2.13 μm (right).

Fig. 9. Lookup tables using 0.65 and 2.13 μm reflectances for homogeneous and inhomogeneous cloud models. μ_0=0.65, μ=1.0 and φ - φ_0 = 0°.

Fig. 10. MODIS granule image (RGB=band 4:3:1) from Terra on April 17, 2007, and MODIS cloud mask (upper panels). The comparisons of retrieved ice cloud optical thicknesses from homogeneous and inhomogeneous ice crystals (middle panels). The comparisons of retrieved ice cloud effective particle sizes from homogeneous and inhomogeneous ice crystals (bottom panels).

Fig. 11. Effective particle sizes for inhomogeneous ice crystals.

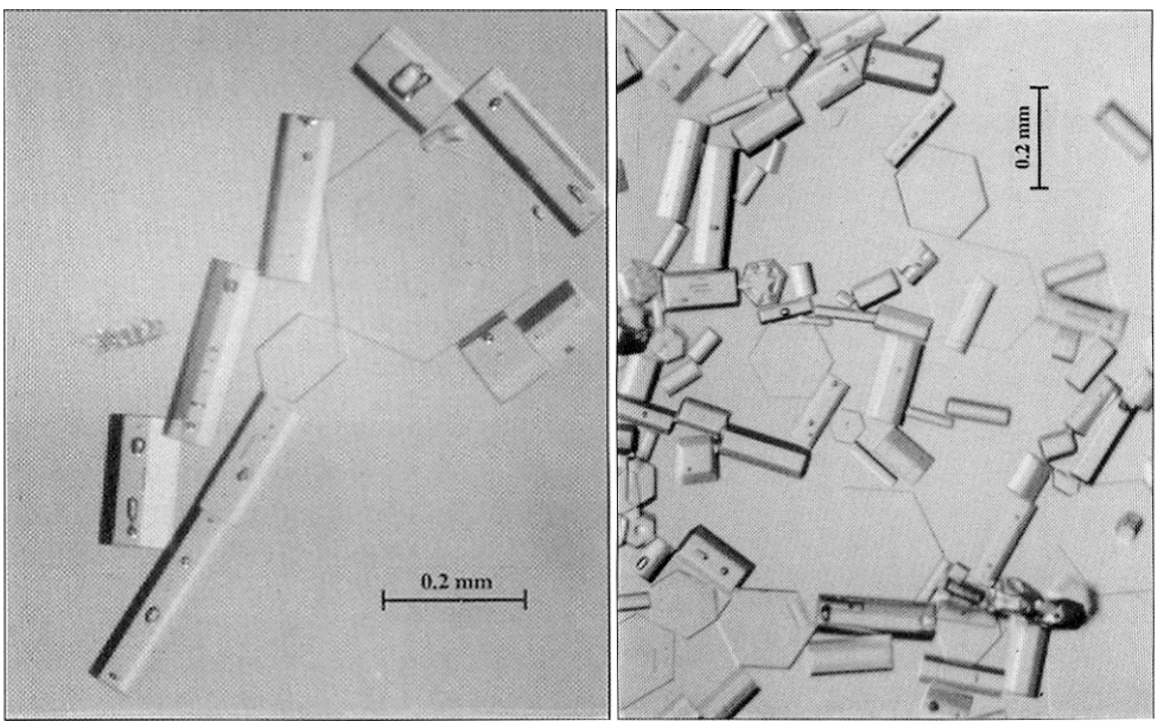

Fig. 1. Inhomogeneous ice crystals sampled by Walter Tape [Tape, 1994] at the South Pole, on January 19, 1985 (left) and January 17, 1986 (right).

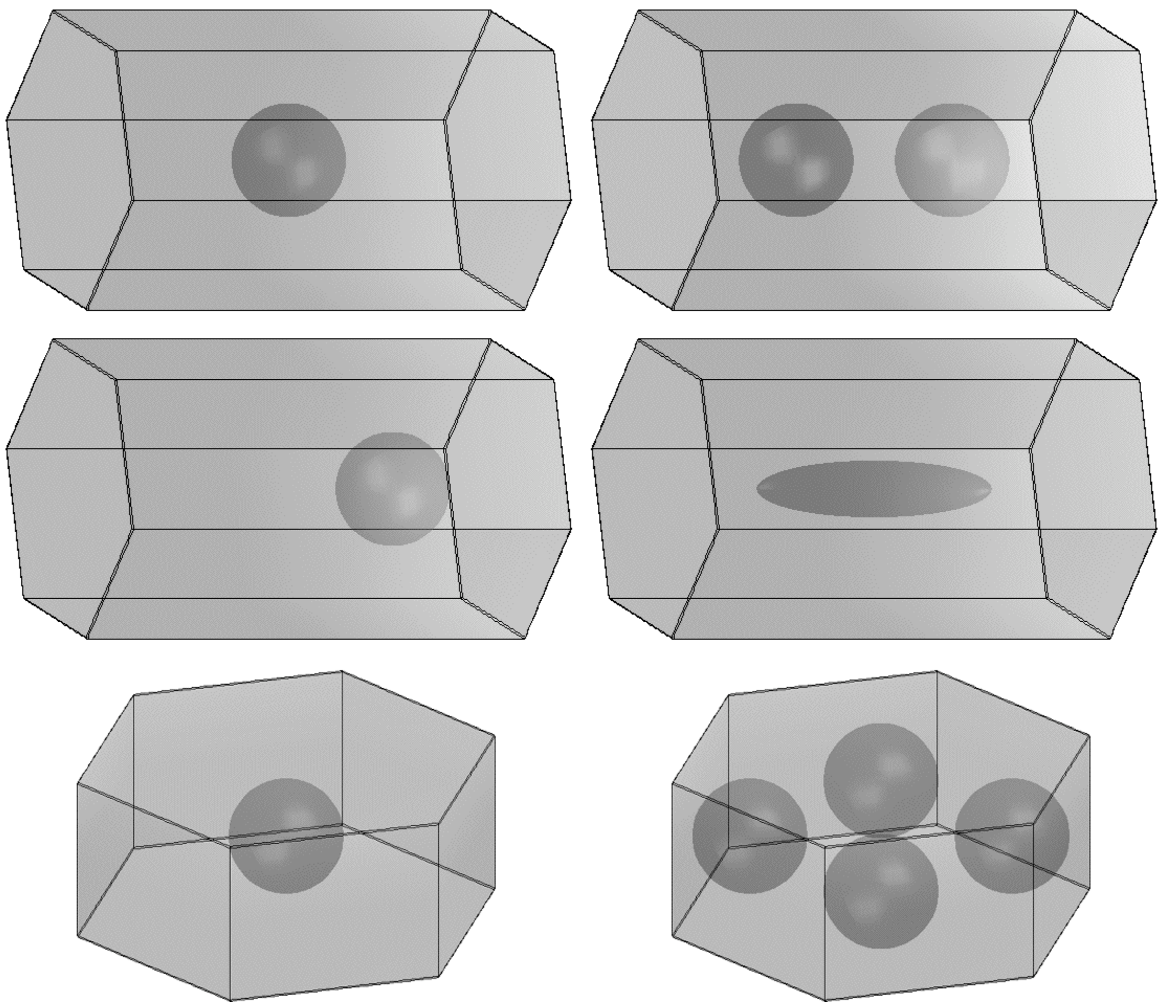

Fig. 2. The geometries of inhomogenous ice crystals.

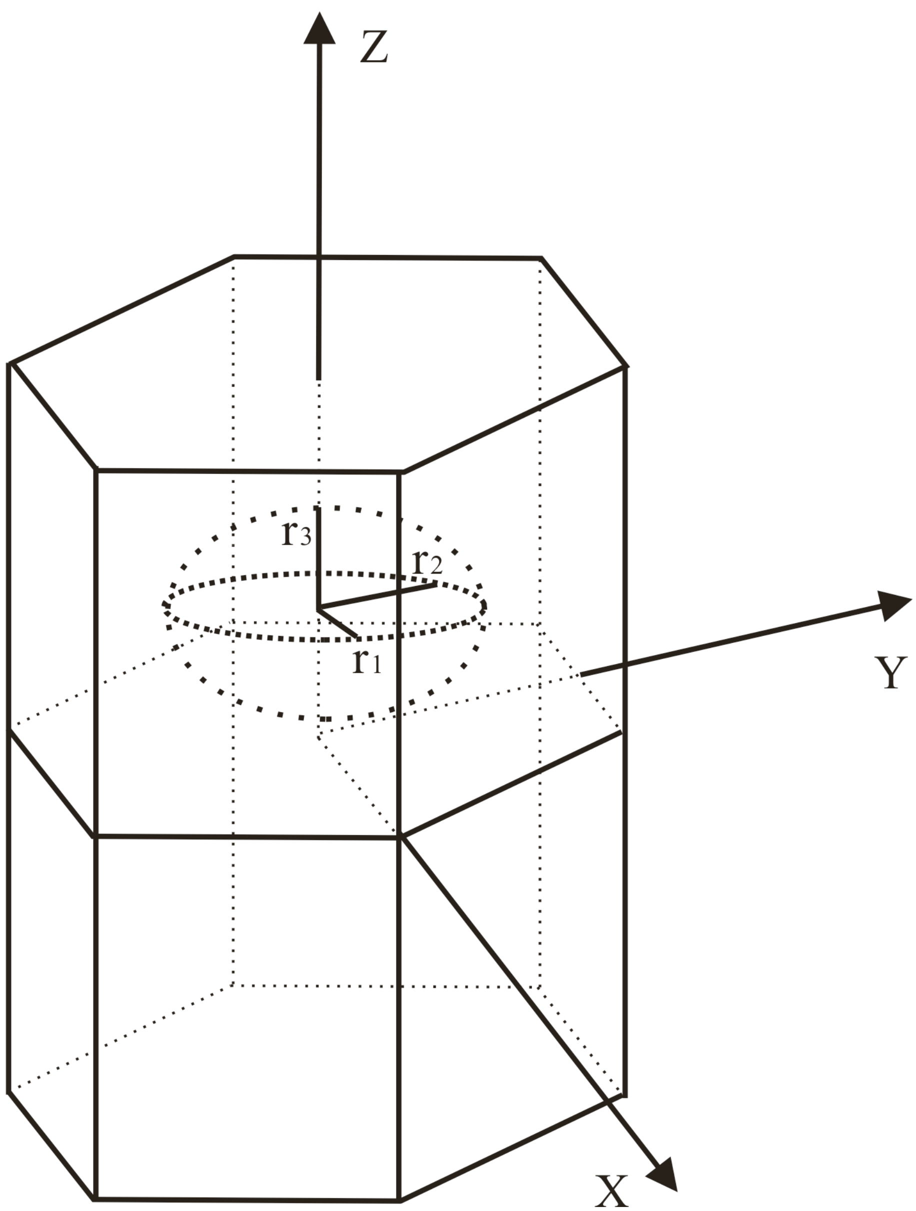

Fig. 3 Geometry of a hexagonal ice crystal with an air bubble inside.

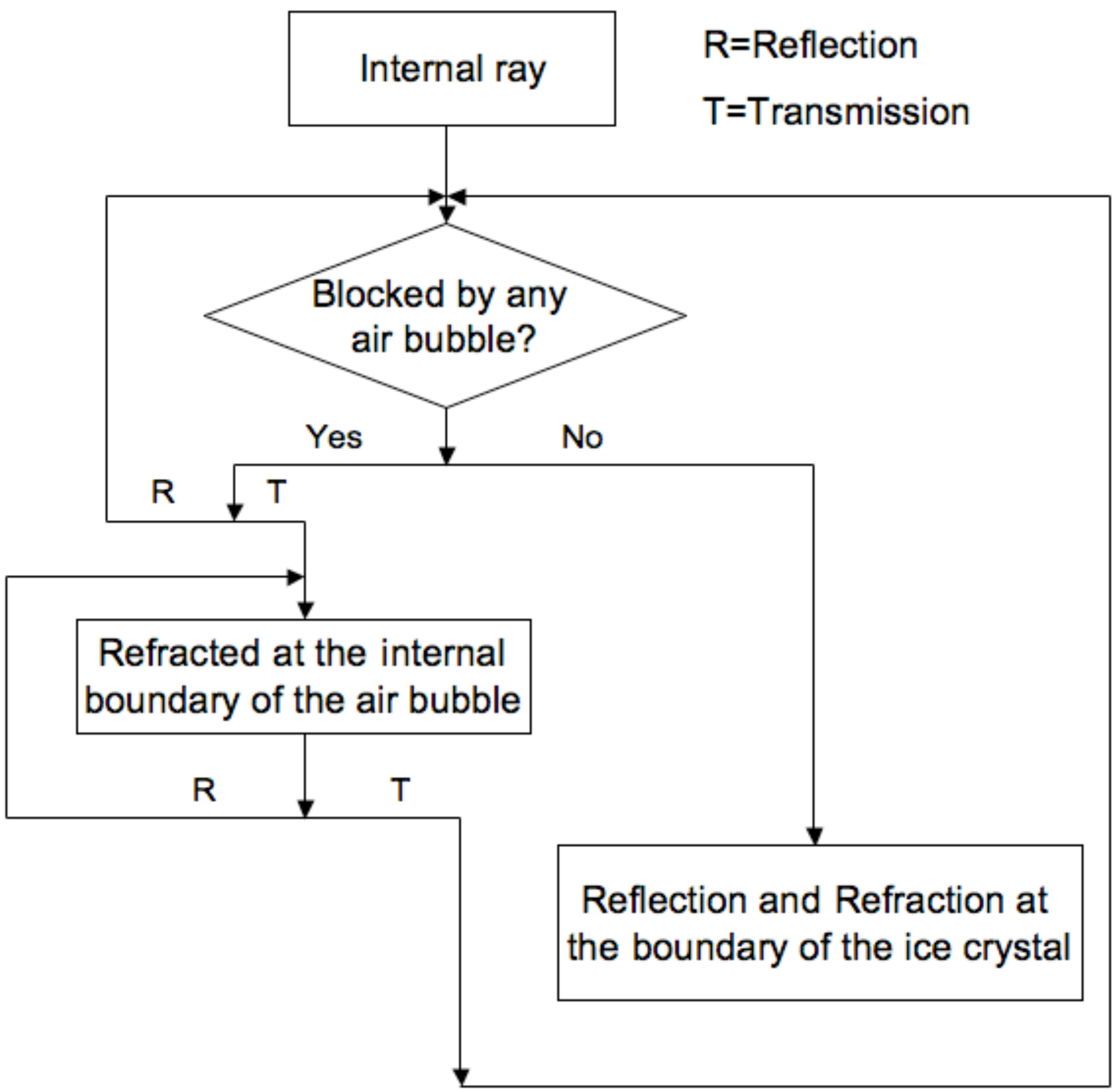

Fig. 4. Schematic flow-chart for reflection and refraction by internal air bubbles.

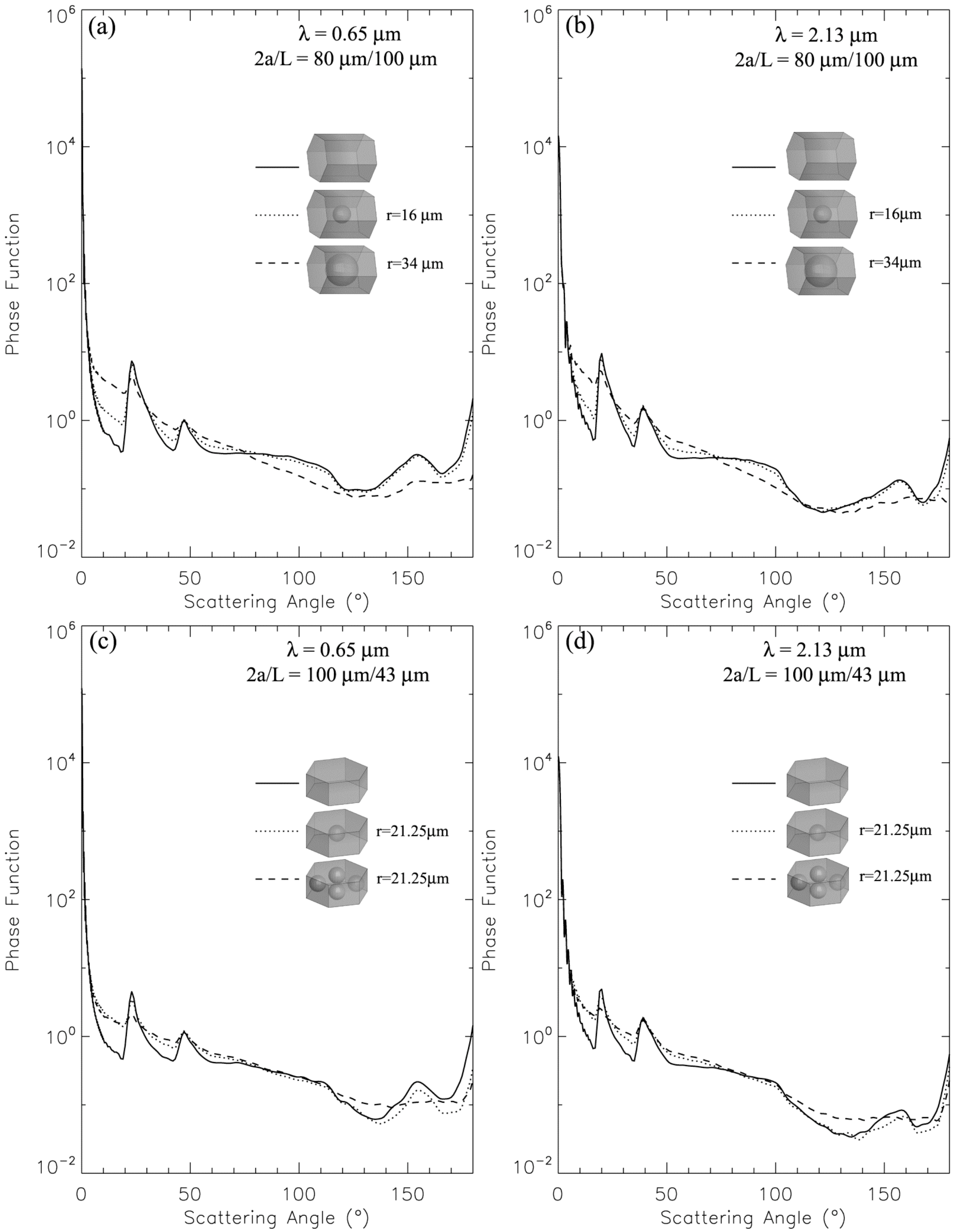

Fig. 5. Scattering phase functions for homogeneous and inhomogeneous ice crystals at λ=0.65 μm (panels a and c) and 2.13 μm (panels b and d).

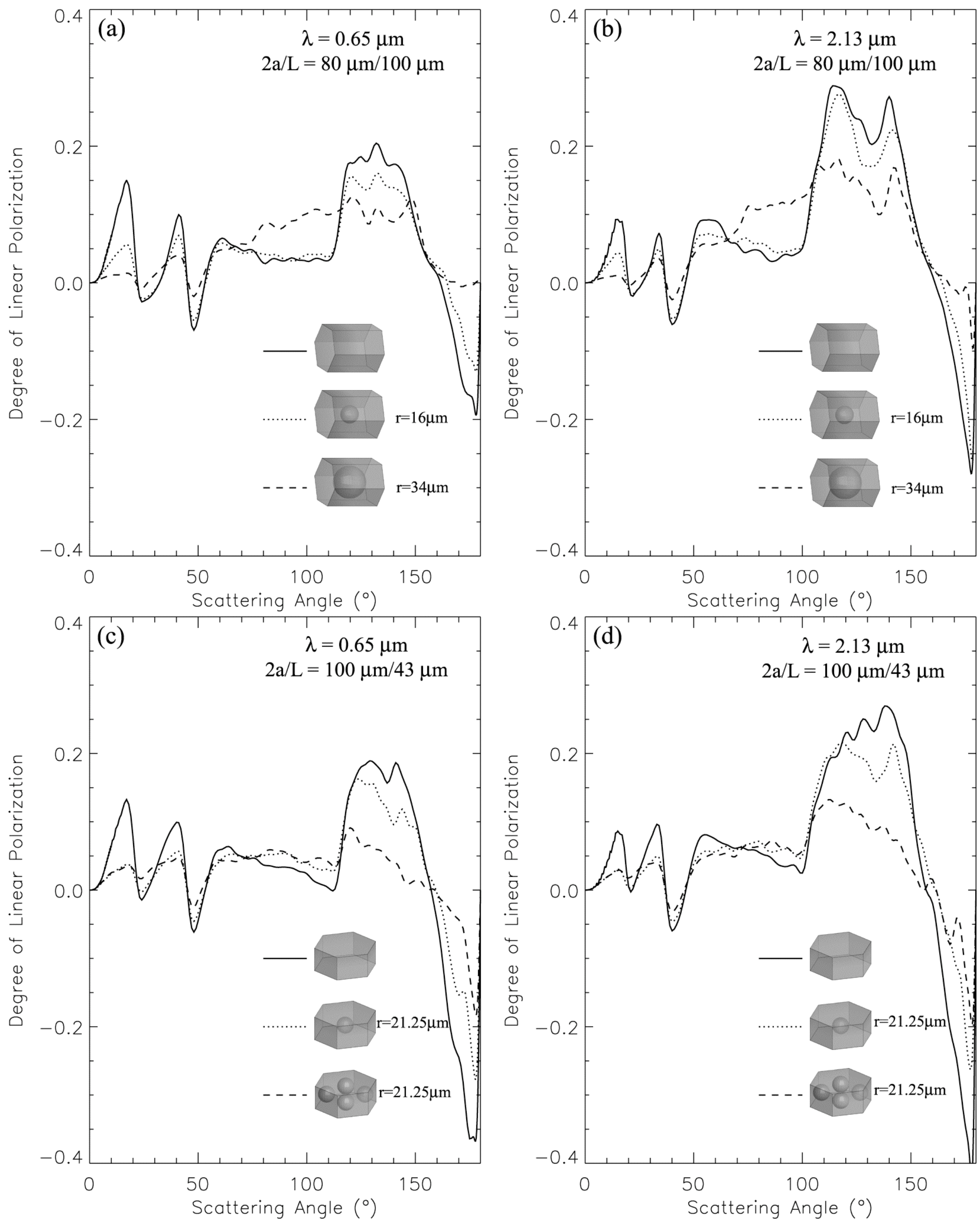

Fig. 6. Degrees of linear polarization for homogeneous and inhomogeneous ice crystals at λ=0.65 μm (panels a and c) and 2.13 μm (panels b and d). The ice crystals' sizes and morphologies in this figure are the same as those in Fig. 5.

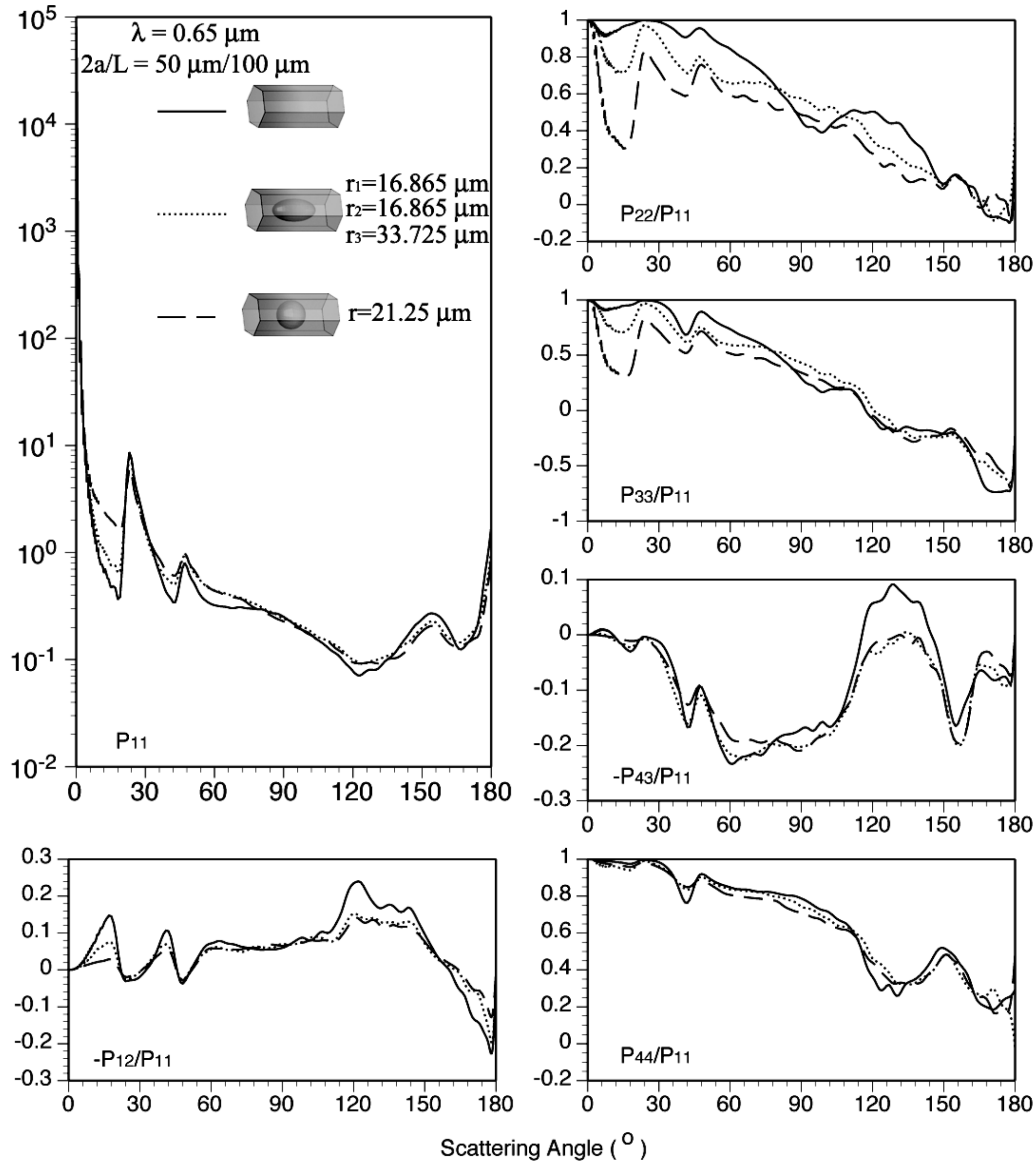

Fig. 7. Scattering phase matrixes for homogeneous and inhomogeneous ice crystals at λ=0.65 μm.

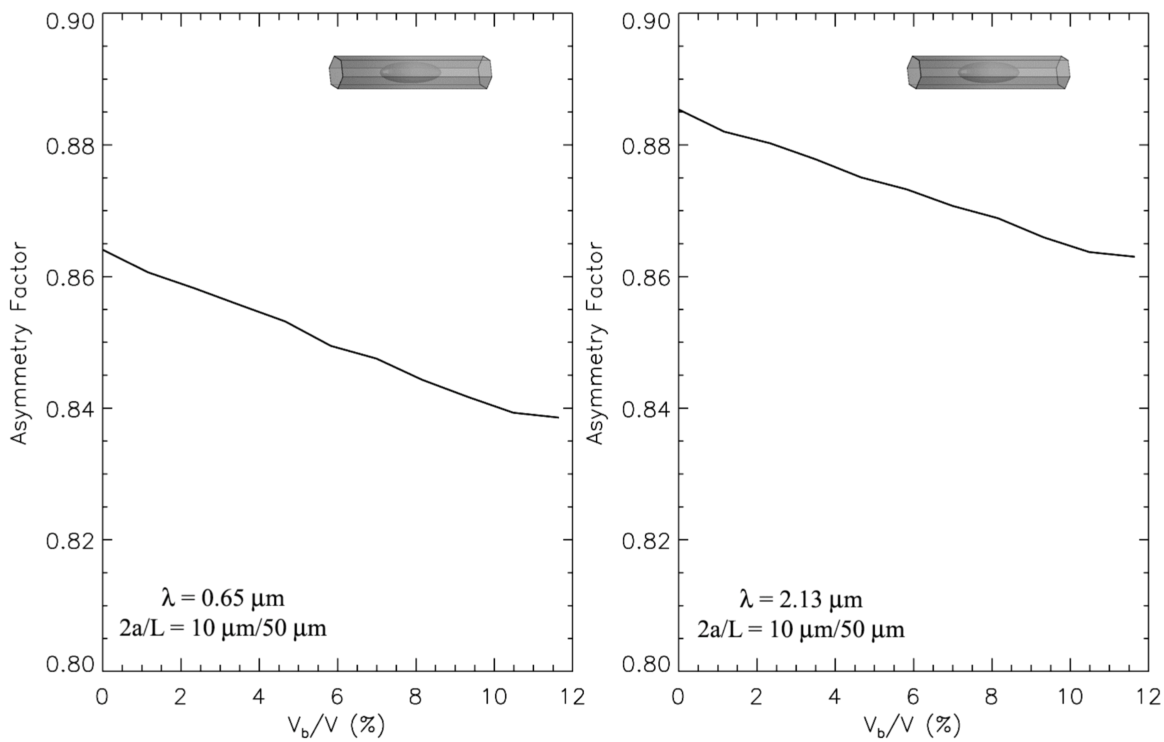

Fig. 8. Asymmetry factors for inhomogeneous ice crystals at λ=0.65 μm (left) and 2.13 μm (right).

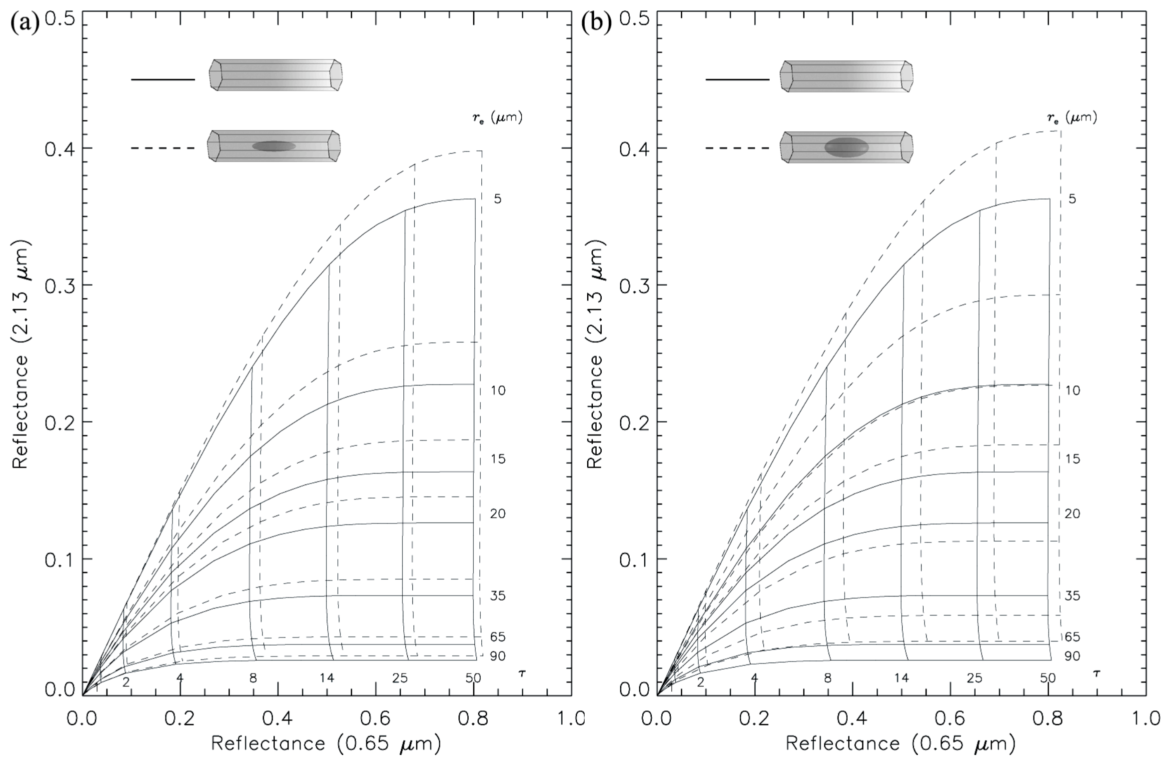

Fig. 9. Lookup tables using 0.65 and 2.13 μm reflectances for homogeneous and inhomogeneous cloud models. μ_0=0.65, μ=1.0 and φ - φ_0 = 0°.

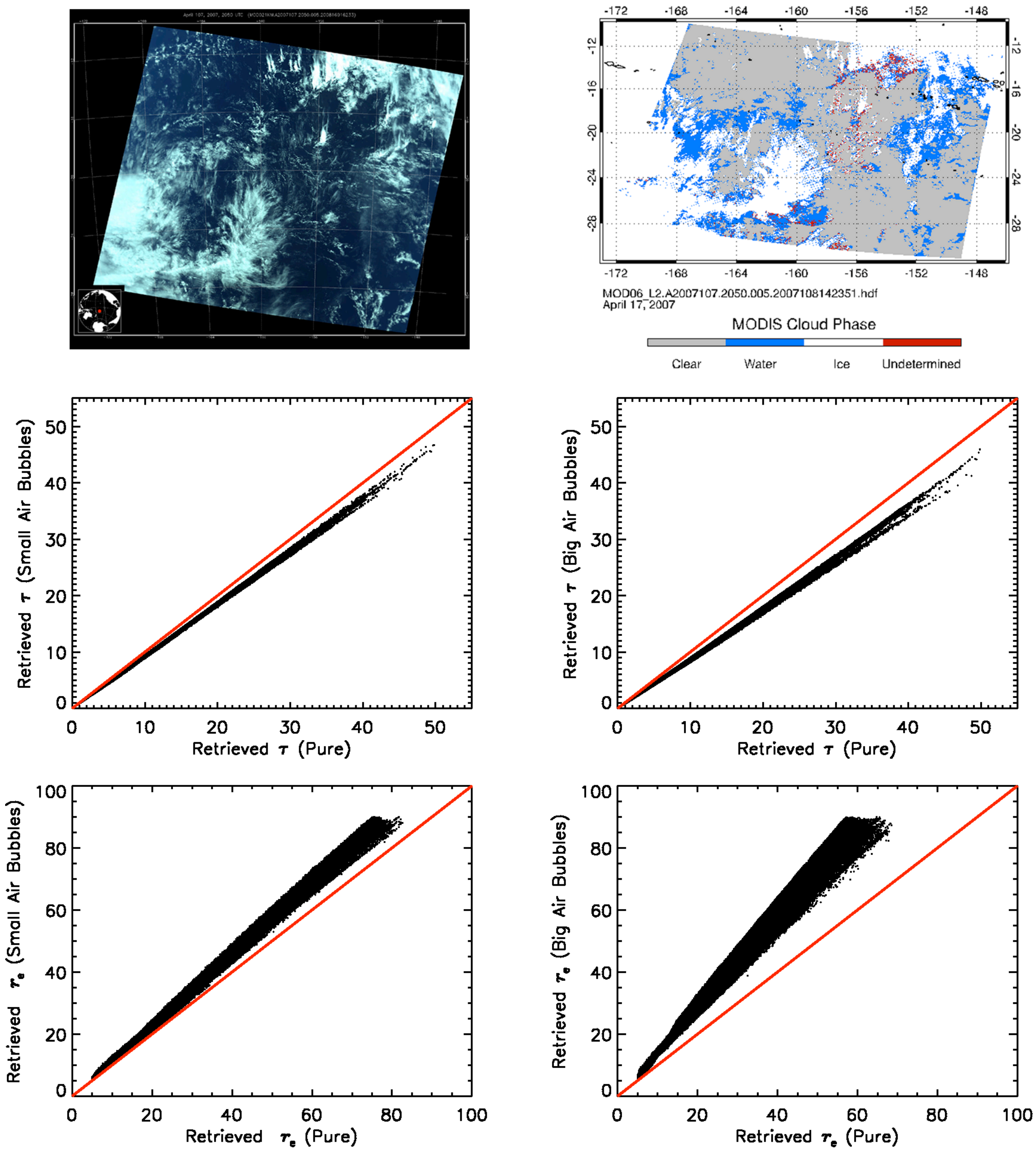

Fig. 10. MODIS granule image (RGB=band 4:3:1) from Terra on April 17, 2007, and MODIS cloud mask (upper panels). The comparisons of retrieved ice cloud optical thicknesses from homogeneous and inhomogeneous ice crystals (middle panels). The comparisons of retrieved ice cloud effective particle sizes from homogeneous and inhomogeneous ice crystals (bottom panels).

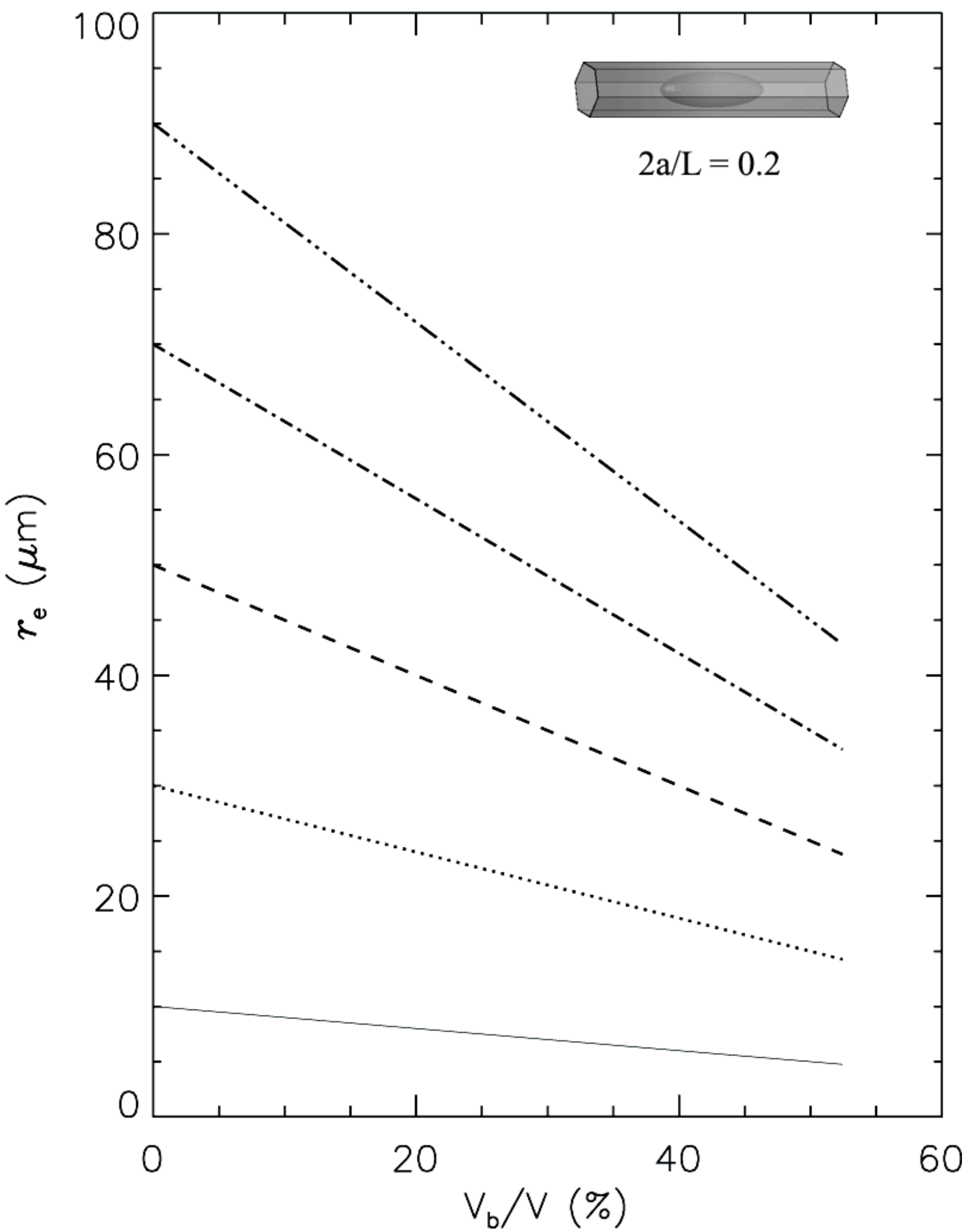

Fig. 11. Effective particle sizes for inhomogeneous ice crystals.